



Interfacial engineering-induced Janus heterostructures with enhanced electronic regulation for efficient oxygen electrocatalysis in rechargeable Zn-air batteries

Jie Zhang ^a, Xinran Dong ^a, Gang Wang ^{a,b}, Jinwei Chen ^{a,b}, Ruilin Wang ^{a,b,*}

^a College of Materials Science and Engineering, Sichuan University, Chengdu 610065, China

^b Engineering Research Center of Alternative Energy Materials & Devices, Ministry of Education, Sichuan University, Chengdu 610065, China



ARTICLE INFO

Keywords:

Janus heterostructure
Transition-metal sulfide
Interface engineering
Oxygen electrocatalytic reaction
Rechargeable zinc-air battery

ABSTRACT

Construction of efficient non-noble metal electrocatalysts for oxygen reduction reaction (ORR) and oxygen evolution reaction (OER) are extremely important for zinc-air batteries (ZABs). Herein, a novel Janus heterostructure, coupling CeO₂ with bimetallic metal sulfides (ZnCoS) with precise heterointerfaces, was designed through an interfacial engineering-induced strategy. Benefiting from the interfacial synergistic effect, the asymmetric Janus heterostructure of CeO₂/ZnCoS (J-CeO₂/ZCS) exhibits satisfactory ORR and OER activity, in terms of E_{1/2} of 0.87 V for ORR and overpotential of 290 mV for OER. Theoretical calculation further demonstrates that the heterointerface effectively modulates the electronic structure and charge redistribution, thus improving redox reactivity of active sites and the absorption/desorption of reaction intermediates. When the J-CeO₂/ZCS applied in liquid and flexible ZABs as air cathodes, the devices deliver excellent power density and cycling stability. This Janus structure of composite catalysts affords a new opportunity for designing efficient oxygen electrocatalysts with heterostructures.

1. Introduction

With the excessive usage of traditional fossil fuels and increasingly serious environmental problems, it is imperative to develop sustainable energy storage and conversion technologies [1,2]. Rechargeable zinc-air batteries (ZABs) with high theoretical specific energy density, zero carbon emissions, and good security are emerged as a promising next-generation energy devices [3,4]. However, the performance of ZABs highly depends on the air cathodes, in which involve the multi-step electron transfer paths and sluggish reaction kinetics of oxygen reduction reaction (ORR) and oxygen evolution reaction (OER) [5]. To date, Pt and Ru-based catalysts have been considered as efficient benchmark catalysts for ORR and OER, respectively [6]. Nevertheless, their high price and scarcity reserves severely suppress the extensive industrial application [7]. Therefore, the development and rational design of cost-efficient and high-performance ORR/OER bifunctional electrocatalyst are highly necessary.

Numerous studies have been made to the transition metal (TM)-based nanomaterials owing to their advantages of abundant resources, low-cost, and considerable physicochemical properties, especially

concentrating on transition metal oxides (TMO) [8], nitrides [9], sulfides (TMS) [10], carbides [11], phosphides [12], and alloyed nanoparticles [13], etc. Moreover, the introduction of carbon matrix has been regarded as an effective way to disperse and protect the metal components. The synergistic effect between carbon and metal components significantly regulates the geometric and electronic structure of the active metal center, thus resulting in an improved catalytic performance. TMSs have attracted considerable attention owing to their rich redox couples could effectively activate/dissociate the oxygen molecules, which is beneficial to enhance the intrinsic activities [14]. However, the less interfacial sites and low electrical conductivity of TMSs have impeded the further improvement on performance [15]. Interface engineering has been utilized to modulate electronic states and enable separate reaction steps to collaboratively accelerate catalysis [16]. Unfortunately, most of the TM compounds/TMS interfaces are the core-shell structures of Co@Co₉S₈ [17], NiO@Co₃S₄ [18], and Co₃S₄ @Co₃O₄ [19], etc. The interfaces and active sites cannot be exposed enough to participate in the electrocatalytic reactions, thereby suppressing the intrinsic activity of composite catalysts. At present, constructing binary sulfides and developing TMS-based heterostructures with controllable

* Correspondence to: College of Materials Science and Engineering, Sichuan University, No.24 South Section 1, Yihuan Road, Chengdu 610065, China.
E-mail address: rl.wang@scu.edu.cn (R. Wang).

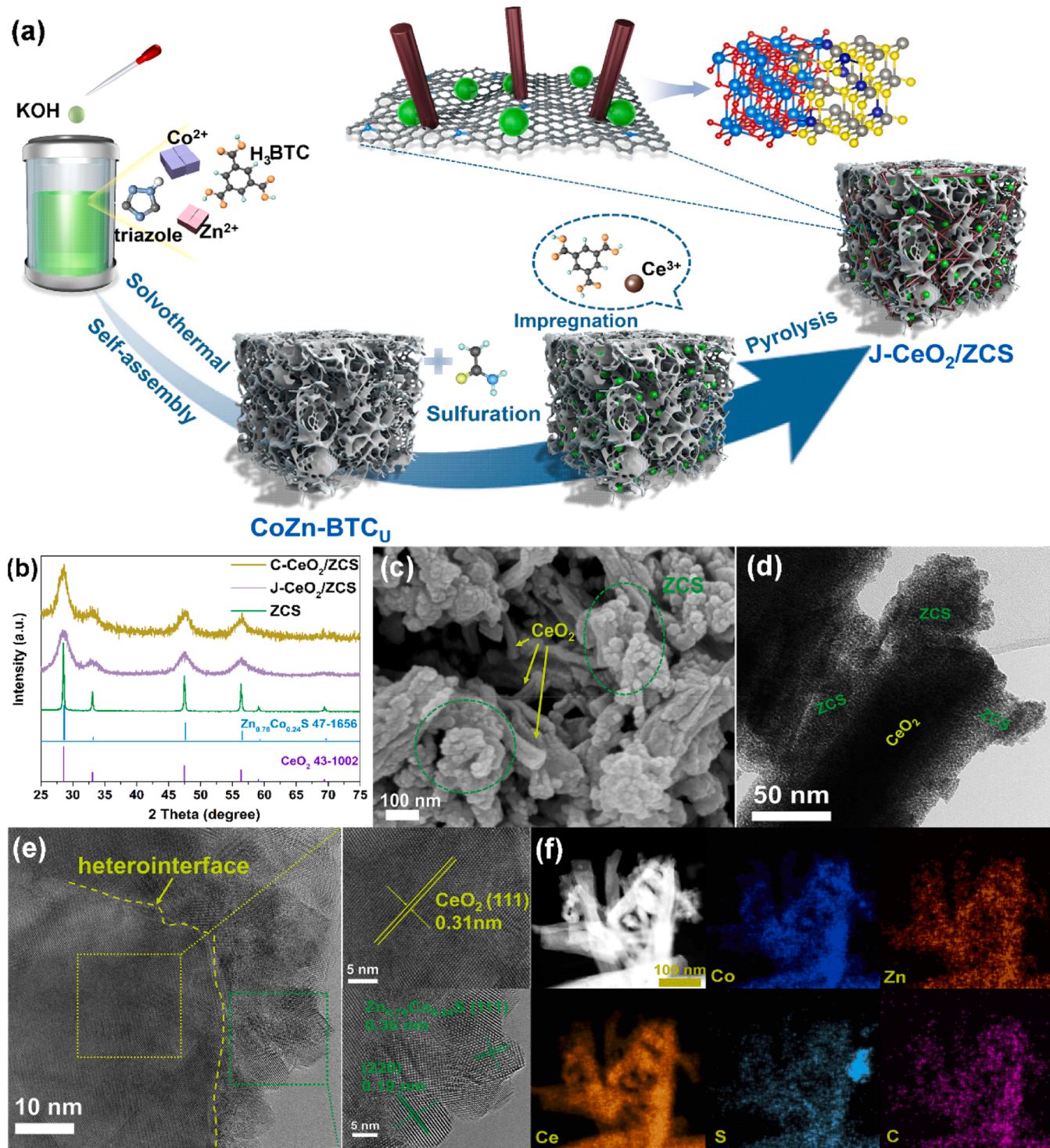


Fig. 1. (a) Schematic illustration of synthetic procedure for J-CeO₂/ZCS. (b) XRD patterns of ZCS, C-CeO₂/ZCS, and J-CeO₂/ZCS. (c-d) SEM images of J-CeO₂/ZCS. (e) HRTEM images and (f) elemental mapping images of J-CeO₂/ZCS.

microstructure have been confirmed to greatly increase the available active sites and improve the charge transfer [20,21]. More importantly, understanding the electron interactions at the coupled interfaces is highly essential to reveal the structure–performance relationship among the diverse constitutions.

Janus heterointerfaces, named after the Roman god Janus, exhibit distinctive electrocatalytic properties due to the anisotropic structures that endowing the controllable physicochemical properties [22]. For instance, the Ni₃N/W₅N₄ electrode with Janus nanostructure displayed

a Pt-like hydrogen evolution reaction (HER) activity and stability, owing to the multilevel structure and the synergistic effect at heterointerface [23]. Another Co/Fe₃O₄ Janus heterojunction with abundant active sites also possessed excellent HER and OER activity, which was attributed to intense electronic interaction of diverse components [24]. Previous studies have demonstrated that Janus nanostructures not only induce synergistically catalysis but also result in stronger electronic interaction and suitable chemical environments at interfaces [25]. Recently, a controllable Janus heterostructures of FeCo/(FeCo)S was also developed

as efficient oxygen electrocatalyst [26]. The heterointerface could generate the interaction, induce the electron transfer between components, and stabilize the active sites [27]. Besides, the synergistic effect of the metallic sites at interfaces could optimize the adsorption/desorption energy of key intermediates, thus improving the ORR and OER performance. However, constructing Janus TM compounds/TMS heterointerfaces still exists technical barriers because it is difficult to elaborately control components and regulate interfaces at the nanoscale. Therefore, Janus TM compounds/TMS heterointerfaces for bifunctional oxygen catalysis are rarely reported even though possess potential applications.

Currently, CeO_2 has been proposed as an efficient promoter due to its extraordinary redox couple ($\text{Ce}^{3+}/\text{Ce}^{4+}$) and abundant oxygen vacancies (O_v), thus providing good redox performance and oxygen storage capacities [28]. Besides, the strong interactions between CeO_2 and other active components endow the composites a highly activity and stability, which is also favorable for the electrocatalytic process [29]. Thus, constructing Janus heterostructures of CeO_2 and TMS system provides possibility to modulate the electronic structure of TMSs and produce additional active species, which may be conducive to achieve high performance of ORR and OER.

Here, we propose the Janus heterointerface by coupling CeO_2 and zinc cobalt sulfide (ZCS) into one entity (CeO_2/ZCS) encapsulated in the carbon layer that derived from the unsaturated metal-organic framework (MOF). Structural characterizations reveal the asymmetric Janus heterostructure of CeO_2/ZCS (J- CeO_2/ZCS). CeO_2 can modify the interface and enrich the O_v , thus altering the electronic states of ZCS and further improving the electrocatalytic activities. The highly distributed ZCS and CeO_2 with porous carbon matrix afford more accessible active sites. Moreover, the strong interfacial effect restrains the loss and aggregation of active species, giving rise to remarkable stability of J- CeO_2/ZCS . Benefiting from this unique Janus heterostructure, the J- CeO_2/ZCS catalyst exhibits superior electrocatalytic activity for ORR and OER, exceeding that of the commercial Pt/C and RuO_2 , respectively. Theoretical calculation verifies that the well-designed heterostructure can effectively regulate the electronic structure of metallic sites, thus improving the redox reactivity and optimizing the reaction paths at the interfaces. As expected, the J- CeO_2/ZCS was further assembled into rechargeable liquid ZABs and flexible ZABs with high efficiency and stability. This study provides a way for the design of Janus heterostructures and gives a guidance on developing efficient bifunctional catalysts for energy devices.

2. Materials synthesis

2.1. Synthesis of CoZn-BTC_U

Typically, the CoZn-BTC_U precursor was synthesized through a solvothermal method. A mixture of $\text{Co}(\text{Ac})_2 \cdot 4 \text{ H}_2\text{O}$ (3 mmol), $\text{Zn}(\text{Ac})_2 \cdot 2 \text{ H}_2\text{O}$ (1 mmol), 1,3,5-Benzenetricarboxylic acid (H_3BTC , 6 mmol), triazole (6 mmol), and KOH (12 mmol) was added into 100 mL of N,N-Dimethylformamide (DMF). The mixture was ultrasonicated and then kept reaction at 160 °C for 24 h with continuously stirring, followed by naturally cooling to room temperature. The precipitates were collected by centrifugation, wash, and vacuum-dried at 60 °C, which was named as CoZn-BTC_U .

For comparison, Co-BTC was prepared according to the same procedure as CoZn-BTC_U but without the addition of triazole and KOH. Co-BTC was also prepared but without the addition of triazole, KOH, and $\text{Zn}(\text{Ac})_2 \cdot 2 \text{ H}_2\text{O}$.

2.2. Synthesis of ZCS

100 mg of CoZn-BTC_U precursor and 7.5 mmol thioacetamide were dispersed in 50 mL of ethanol under sonication for 30 min to obtain homogeneous solutions, respectively. Then, two solutions were mixed

and stirred at 90 °C for 2 h. When naturally cooled to room temperature, the black precipitates were washed with ultrapure water and ethanol for several times and then vacuum-dried at 60 °C overnight. The obtained zinc cobalt sulfides were abbreviated as ZCS.

2.3. Synthesis of J- CeO_2/ZCS

100 mg of ZCS was dispersed in 15 mL of ethanol under sonication for 30 min. $\text{Ce}(\text{NO}_3)_3 \cdot 6 \text{ H}_2\text{O}$ (0.2 mmol) and H_3BTC (0.2 mmol) was dissolved in the mixture of 25 mL of distilled water with 15 mL ethanol and stirred for 30 min. After that, the two solutions were mixed and heated at 90 °C for 2 h with continuously stirring. After that, the precipitate was washed and vacuum-dried at 60 °C overnight. The collected products were pyrolyzed at 600 °C in Ar atmosphere for 2 h with the heating rate of 5 °C min⁻¹ to obtain the Janus heterostructure of 0.2 CeO_2/ZCS (abbreviated as J- CeO_2/ZCS in what follows). To further investigate the influence of CeO_2 contents, 0.1 CeO_2/ZCS and 0.3 CeO_2/ZCS were also prepared in the similar method by changing the amounts of $\text{Ce}(\text{NO}_3)_3 \cdot 6 \text{ H}_2\text{O}$ as 0.1 mmol and 0.3 mmol, respectively.

In addition, individual CeO_2 was synthesized according to the above-mentioned method, except there was no addition of ZCS during the first step. Conventional CeO_2/ZCS (named as C- CeO_2/ZCS) was also synthesized by using the same procedure as C- CeO_2/ZCS but changing the CoZn-BTC_U as CoZn-BTC .

Characterizations methods and computational methodology are provided in [Supporting Information](#).

3. Results and discussion

3.1. Structural and morphological characterization

The synthesis procedure of J- CeO_2/ZCS catalyst is displayed in [Fig. 1a](#). With the assistant of triazole and KOH, the unsaturated CoZn-MOF (CoZn-BTC_U) was synthesized by using Co and Zn ions assembled with H_3BTC . Specially, KOH reacted with a part of rigid BTC^{3-} ligand, bringing about the coordinately unsaturated metal sites. For comparison, X-ray powder diffraction (XRD) analysis was conducted to reveal the structure of precursors ([Fig. S1](#)). Diffraction peaks of Co-BTC are in agreement with the previous report, confirming the isostructural Co-MOF (CCDC 245714) [30]. XRD pattern of CoZn-BTC approximately coincides with that of Co-BTC , except for small difference on peaks due to the formation of additional Zn-BTC, indicating the bimetallic CoZn-BTC . Compared with that of CoZn-BTC , the decreased intensity and crystalline of CoZn-BTC_U further reveal that the realized more unsaturated coordination through incorporating triazole ligands. It can be attributed to triazole molecules filled the channels via $\pi-\pi$ stacking with the benzene rings of BTC^{3-} in the precursor [31]. The tabular morphology of Co-BTC and CoZn-BTC can be observed on scanning electron microscopy (SEM) images ([Fig. S2a-b](#)). Notably, the CoZn-BTC_U shows a woven-like loose structure ([Fig. S2c-d](#)).

After sulfidation, CoZn-BTC_U transformed into ZnCoS with the retained loose and porous structure when compared with the ZnCoS derived from CoZn-BTC with dense structure and larger particles ([Fig. S3](#)). The difference on morphology was originated from the diverse structures of precursors that caused by the above-mentioned coordination modes. Besides, its characteristic peaks well match with the standard $\text{Zn}_{0.76}\text{Co}_{0.24}\text{S}$ (JCPDF No. 47-1656) ([Fig. 1b](#)). For both C- CeO_2/ZCS and J- CeO_2/ZCS , the diffraction peaks at 28.5°, 33.1°, 47.5° and 56.3° correspond to the (111), (200), (220), and (311) planes of CeO_2 , which are extremely similar to the peaks of $\text{Zn}_{0.76}\text{Co}_{0.24}\text{S}$. Thus, the broaden diffraction peaks suggest the coexistence of CeO_2 and $\text{Zn}_{0.76}\text{Co}_{0.24}\text{S}$ in C- CeO_2/ZCS and J- CeO_2/ZCS . Also, CeO_2 was also successfully prepared by direct pyrolysis of Ce-MOF, composing of Ce^{3+} assembled with H_3BTC , which possess one-dimensional rod-like structure ([Fig. S4](#)). During introducing the CeO_2 , the ZCS derived from unsaturated CoZn-BTC_U could offer less steric hindrance and stronger interactions with

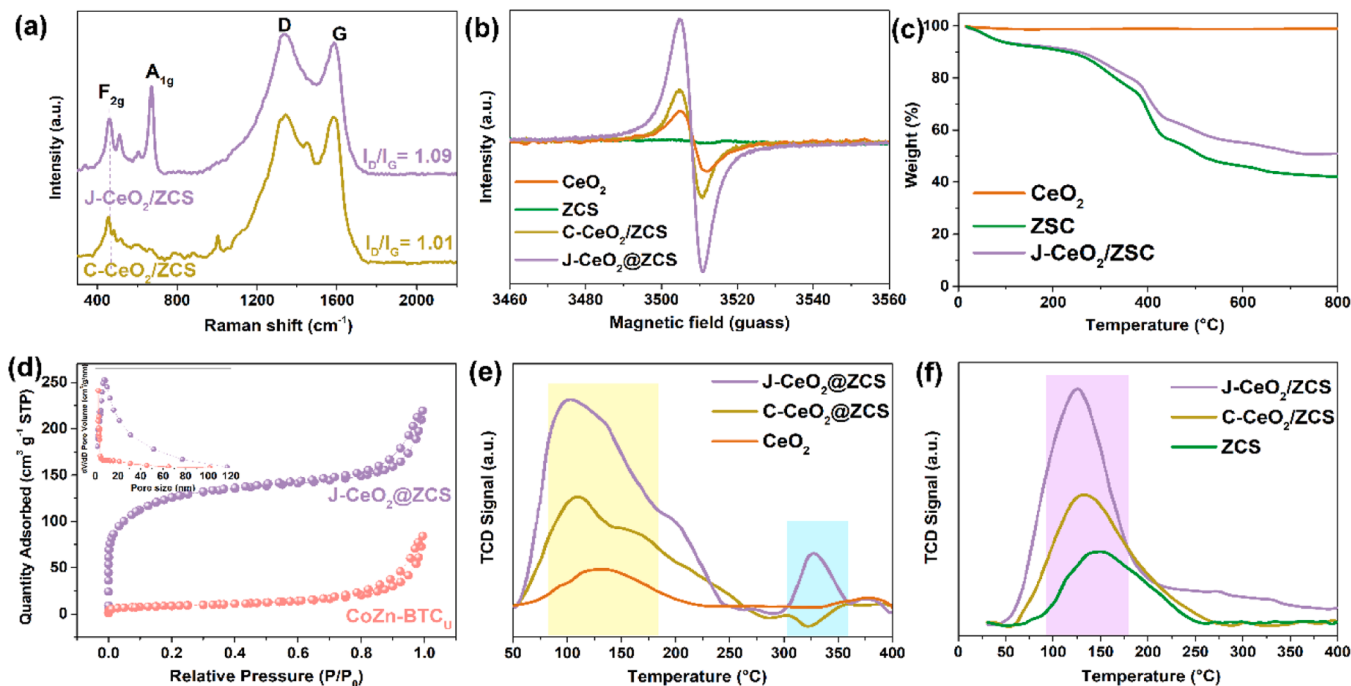


Fig. 2. (a) Raman spectra of C-CeO₂/ZCS and J-CeO₂/ZCS. (b) EPR spectra of CeO₂, ZCS, C-CeO₂/ZCS and J-CeO₂/ZCS. (c) TGA curves of ZCS, CeO₂ and J-CeO₂/ZCS. (d) N₂ adsorption/desorption isotherms of CoZn-BTC_U and J-CeO₂/ZCS, inset: the corresponding pore size distribution. (e) NH₃-TPD and (f) CO₂-TPD profiles of catalysts.

Ce³⁺ diffusion, which makes CeO₂ interlace within the J-ZCS/CeO₂ composite (Fig. 1c). By contrast, CeO₂ nanorods mainly grew on the outside of the ZCS particles derived from CoZn-BTC, showing the weak interaction between CeO₂ and ZCS in the C-ZCS/CeO₂ (Fig. S5). As shown in Fig. 1d, CeO₂ nanorods evenly encapsulated in ZCS nanostructures, which is beneficial to realize interfacial engineering of ZCS/CeO₂ heterostructure. d high-resolution transmission electron microscopy (HRTEM) images further confirm the presence of heterointerface with distinctly crystal structures (Fig. 1e). The lattice fringe spacing of 0.31 nm suggests the (111) plane of CeO₂. The interplanar crystal spacings of 0.19 and 0.36 nm correspond to the (220) and (111) planes of Zn_{0.76}Co_{0.24}S, respectively. It is clear that ZCS and CeO₂ intersect with each other, and the so-called Janus heterointerface is formed. Benefiting from the low steric hindrance and unique structure, the ZCS and CeO₂ kept stable after pyrolysis and thus forming Janus heterostructure of CeO₂/ZCS. Such a heterointerface can facilitate the electronic regulation between different domains, which not only enhances the electrical conductivity and structural stability, but also exposes more reactive active sites [32]. Elemental mapping images (Fig. 1f) indicate the homogeneous distribution of Co, Zn, Ce, S, and C elements throughout the nanocomposite. The corresponding energy dispersive X-Ray (EDX) spectrum verify that the molar ratio of the Co atom to Zn atom is approximately 1/3 (Fig. S6), which is in accordance with the XRD result (Zn_{0.76}Co_{0.24}). However, the molar ratio of S atom in J-CeO₂/ZCS is much lower than that in standard Zn_{0.76}Co_{0.24}S phase, further indicating the high concentration of sulfur vacancies.

Raman analyses were used to confirm the structural information and nature of carbon in J-CeO₂/ZCS. As shown in Fig. 2a, two intense characteristic peaks at ~1342 and 1588 cm⁻¹ correspond to the typical D and G bands, attributed to the structural disorder/defects on carbon plane and the stretching vibration of sp²-C atoms, respectively [33]. Notably, the I_D/I_G value of J-CeO₂/ZCS is calculated to be 1.09, which is higher than that of C-CeO₂/ZCS (1.01). It implies that more structural defects and lattice distortions formed in the J-CeO₂/ZCS, which can be considered as additional active sites to further improve the electrocatalytic performance by optimizing the adsorption of reaction

intermediate [34]. Besides, the typical F_{2g} mode at ~464 cm⁻¹ for CeO₂ is observed, which is in accord with XRD results. As for the J-CeO₂/ZCS, the band at 668 cm⁻¹ belongs to the metal-S vibration mode of zinc cobalt sulfide. Compared with C-CeO₂/ZCS, the A_{1g} mode and slight positive shift of F_{2g} on J-CeO₂/ZCS suggest more exposed active sulfide species and electron transfer between ZCS and CeO₂, which is induced by the interfacial engineering. In order to verify the vacancy concentration, electron paramagnetic resonances (EPR) information was recorded (Fig. 2b). J-CeO₂/ZCS exhibits a higher signal relative to CeO₂, ZCS, and C-CeO₂/ZCS, demonstrating the oxygen vacancies together with interfacial sulfur vacancies. Especially, the interfacial sulfur vacancies were attributed to a certain amount of S atoms thermally transferred to precursor during the pyrolysis process for producing CeO₂. The interfacial vacancies can act as electrochemical active sites to actuate OER and ORR, which is conductive to the bifunctional activity [35]. Based on Raman and EPR results, subtle lattice distortions and abundant vacancies appeared at the interface could maximize the exposure of catalytic sites and thus optimize the catalytic property [36].

Thermal stability was exemplified by thermogravimetric analysis (TGA), which also can be applied to estimate percentages of ZCS and CeO₂ in the J-CeO₂/ZCS. CoZn-BTC_U shows poor thermal stability before 500 °C due to the fast collapse after being heated (Fig. S7). In terms of J-CeO₂/ZCS, the stage from room temperature to 100 °C was caused by the loss of surface water (Fig. 2c) [39], leading to the weight loss of ~6 wt%. The weight loss appeared at ~270 °C is ascribed to the decomposition of carbon, further confirming that the nitrogenous organic ligands converted into the N-doped carbon. TGA curves also indicate that the compositions of active CeO₂ and ZCS are approximately 9 and 42 wt% in J-CeO₂/ZCS, respectively, which is estimated according to the thermostable CeO₂ (kept stable until 800 °C). Fig. 2d shows the N₂ adsorption/desorption isotherms of J-CeO₂/ZCS and CoZn-BTC_U, revealing the calculated specific surface areas of 445.5 and 31.9 m² g⁻¹, respectively. The typical type-IV isotherm with a hysteresis loop also indicates the mesoporous characteristic of J-CeO₂/ZCS [37]. Pore size distribution (inset of Fig. 2d) further verify the dominant mesopores in J-CeO₂/ZCS with very few macropores. The hierarchical architecture of

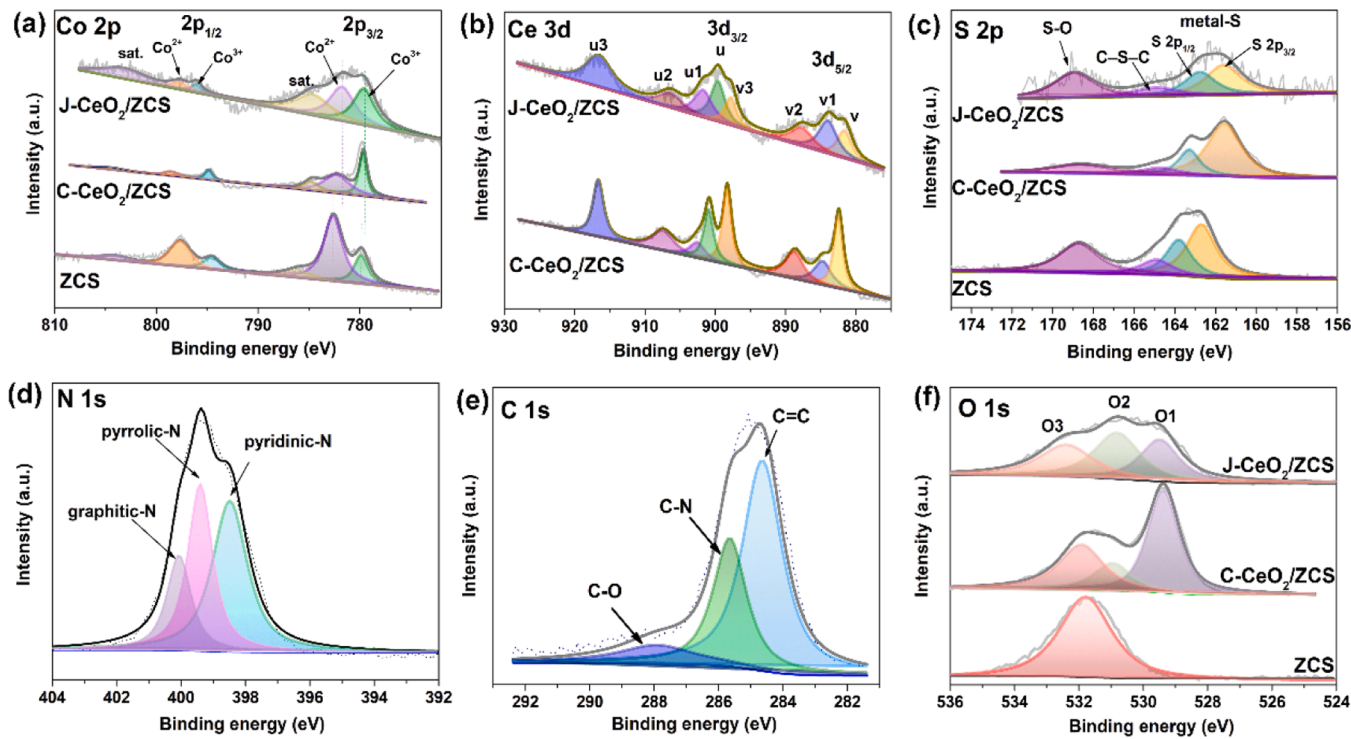


Fig. 3. High-resolution XPS spectra of (a) Co 2p, (b) Ce 3d, (c) S 2p, (d) N 1s, and (e) C 1s, and (f) O 1s in the selected catalysts.

J-CeO₂/ZCS expand the catalyst/electrolyte interfaces, expose more active sites to access the oxygen-relevant species and accelerate the mass transfer of reaction species [38].

NH₃-temperature programmed desorption (TPD) and CO₂-TPD were conducted to evaluate the basicity and acidity. NH₃-TPD curves of catalysts desorbed at different temperatures were shown in Fig. 2e. Two intense desorption peaks on J-CeO₂/ZCS correspond to the Brønsted acid site (< 300 °C) and Lewis acid sites (> 300 °C), respectively [39]. The higher signal of J-CeO₂/ZCS suggests the higher density of Brønsted acid sites, which is beneficial to the activation of O₂ [40]. We speculated that vacancies could regulate the coordination structure of J-CeO₂/ZCS, thus affording acid sites induced by the surface unsaturated Co and Zn atoms. The higher signal intensity in CO₂-TPD curve reveals the higher density of Lewis base on J-CeO₂/ZCS (Fig. 2f). Moreover, the lower desorption temperature means the strength of basicity and acidity on J-CeO₂/ZCS were relatively weaker. Thus, we can speculate that abundant Lewis acid-base pair can be generated on the J-CeO₂/ZCS, which is catalytically active and beneficial to the oxygen electrocatalytic activities.

X-ray photoelectron spectroscopy (XPS) were conducted to acquire surface chemical elemental states of materials [41]. The survey spectrum confirms the presence of Ce, Co, Zn, S, N, C, and O in the J-CeO₂/ZCS (Fig. S8). The surface atomic percentages of the elements are displayed in Table S1. The comparison of Co 2p high-resolution spectra (Fig. 3a) reveal that four kinds of Co species correspond to Co³⁺ peaks in Co 2p_{3/2} and Co 2p_{1/2} as well as the Co²⁺ peaks, which can be well attributed to the Co-S bonding [42]. The binding energies of Co 2p_{3/2} for J-CeO₂/ZCS exhibit negative shifts compared with those of C-CeO₂/ZCS and ZCS, indicating the stronger electronic coupling and electron transfer between sulfides and CeO₂. Zn 2p spectra (Fig. S9) show the binding energies at ~1046 eV (Zn 2p_{1/2}) and ~1023 eV (Zn 2p_{3/2}), which corresponds to the Zn²⁺. Ce 3d spectrum (Fig. 3b) show a multiple splitting composed of Ce³⁺ (u1 and v1) and Ce⁴⁺ (u3), indicating the coexistence of Ce³⁺ and Ce⁴⁺ [43]. Besides, the J-CeO₂/ZCS possesses a larger proportion of Ce³⁺ (30%) in comparison to that in C-CeO₂/ZCS (14%). The above results indicate that oxygen spillover may occur at the interfaces between CeO_x (1.5 < x ≤ 2) and ZCS, which

is favorable for increasing the active oxygen (O⁻) density and improving ORR activity [44]. As for the S 2p spectrum (Fig. 3c), the peaks appeared at 168.9 eV refer to the oxidized S species (S-O) [45]. The peaks located at 160–164 eV clarifies the existence of metallic sulfides, assigning to S 2p_{3/2} and S 2p_{1/2} of metal-S. The peak position slightly shifted towards lower energy, which further confirms the stronger electronic interaction and chemical coupling in J-CeO₂/ZCS [46]. It also may lead to the charge redistribution in the heterointerface between Zn_{0.76}Co_{0.24}S and CeO₂. Additionally, the fitted peak at 164.9 eV are assigned to C-S-C, verifying the successful S doping into carbon [47]. N 1s spectrum (Fig. 3d) was fitted into three kinds of nitrogen species, which are corresponded to pyridinic-N (398.0 eV), pyrrolic-N (399.4 eV), and graphitic-N (400.1 eV), respectively [48]. Generally, the graphitic-N and pyridinic-N can act as additional active sites and modulate the chemical/electronic environment of carbon atoms, further facilitating the ORR process [49]. C 1s spectrum (Fig. 3e) was divided into C=C (284.5 eV), C-N (285.6 eV), and C-O (287.9 eV), which also confirms the successful N doping into carbon [50]. O 1s spectrum of J-CeO₂/ZCS (Fig. 3f) can be divided into O1, O2, and O3, which are assigned to the lattice oxygen (M-O), oxygen vacancies, and hydroxy/S-O species, respectively [51]. Impressively, J-CeO₂/ZCS possesses much higher proportion of O2 (39%) than that in C-CeO₂/ZCS (17%), demonstrating abundant oxygen vacancies generated. By contrast, only O3 peak can be observed on the ZCS, which was caused by the adsorption of the solvent or a small number of oxidized S.

3.2. Electrochemical catalytic property

Cyclic voltammograms (CVs) were measured to preliminarily evaluate the ORR performance of catalysts (Fig. S10). The J-CeO₂/ZCS displays a distinct cathodic peak (0.81 V vs. RHE) in O₂-saturated 0.1 M KOH, reflected the excellent ORR activity, while that exhibits quasi-rectangular feature in Ar-saturated electrolyte. CV results reveal the enhanced ORR activity originates from the synergistic effect of ZCS and CeO₂. LSV curves of catalysts and Pt/C are recorded to further evaluate ORR performance, as shown in Fig. 4a. The onset potential (E_{onset}) and

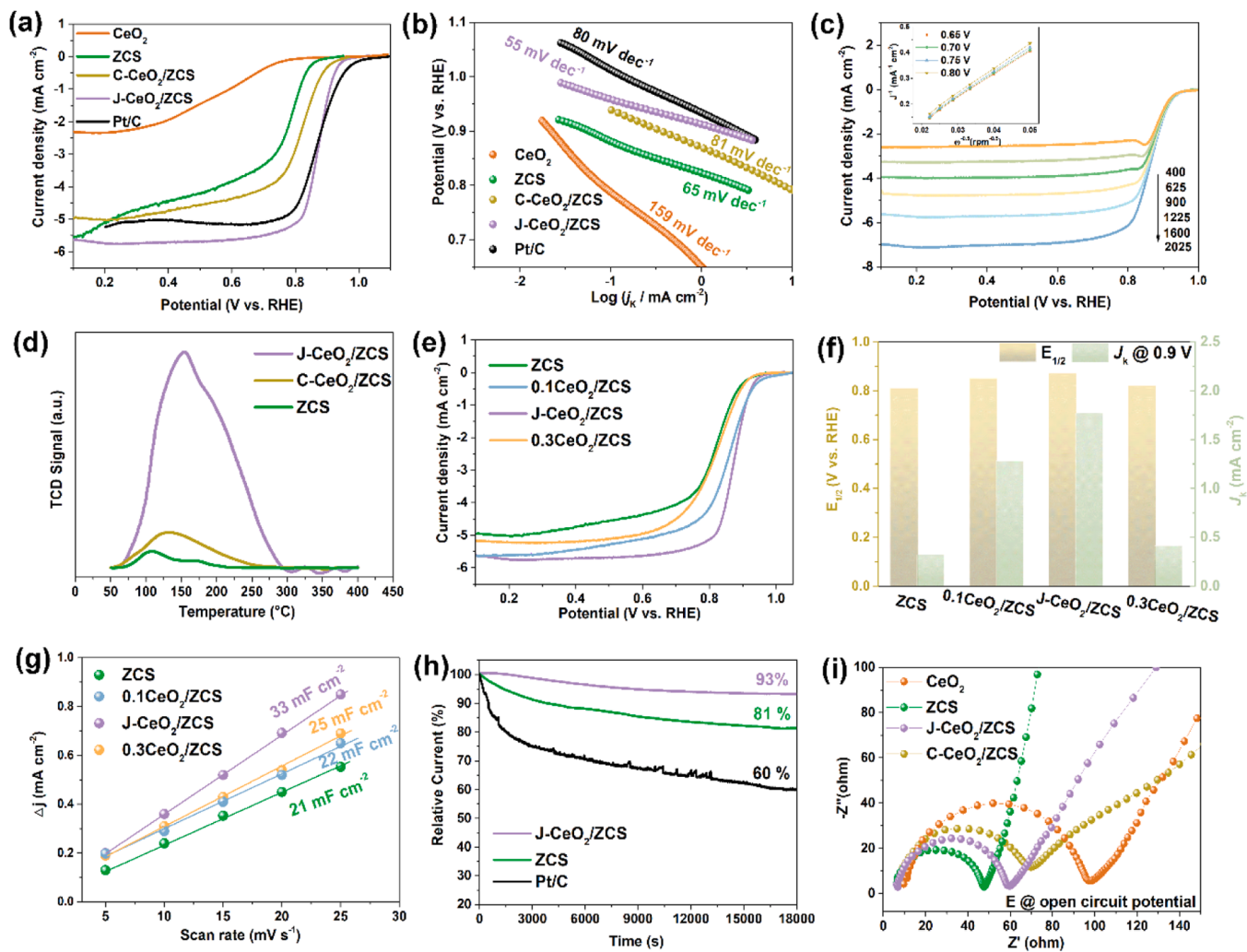


Fig. 4. (a) ORR LSV curves of as-prepared catalysts and Pt/C in 0.1 M O₂-saturated KOH, 10 mV s⁻¹, 1600 rpm. (b) the corresponding Tafel plots. (c) Polarization curves of the J-CeO₂/ZCS with various rotation speeds. (d) O₂-TPD profiles of catalysts. (e) LSV curves of catalysts with various CeO₂ contents and (f) the comparison of E_{1/2} and J_k at 0.9 V. (g) the C_{dl} obtained by CV at different scan rates. (h) Chronoamperometric curves of catalysts recorded at 0.7 V. (i) EIS spectra of catalysts.

half-wave potential (E_{1/2}) of J-CeO₂/ZCS are 0.95 V and 0.87 V, respectively, which is superior than those of Pt/C, C-CeO₂/ZCS, CeO₂ and ZCS as well as other non-noble metal-based ORR electrocatalysts (Table S2). Besides, the stable structure and vacancies can be well maintained after the ORR process (Fig. S11). Among the catalysts prepared with different pyrolysis temperatures, the J-CeO₂/ZCS prepared at 600 °C also exhibits the highest ORR activity, which can be ascribed to the ideal active components of CeO₂ and Zn_{0.76}Co_{0.24}S (Fig. S12). Moreover, Tafel slope is an important indicator for evaluating catalyst, which indicates the charge transfer and kinetics across the catalytic interfaces [52]. The smallest Tafel slope of J-CeO₂/ZCS (55 mV dec⁻¹) suggests a fast ORR kinetic process (Fig. 4b). Furthermore, the limiting current density (J_L) on J-CeO₂/ZCS increases with the increased rotation speeds caused by the decreased oxygen diffusion pathway (Fig. 4c). The electron transfer number (n) was also calculated from the LSV according to the Koutechy-Levich equation (inset of Fig. 4c). The calculated n is approximately 4.0, revealing an efficient 4e⁻ reduction pathway. O₂-TPD can be applied to analyze the enhancement of J-CeO₂/ZCS. As shown in Fig. 4d, J-CeO₂/ZCS possesses a stronger O₂-desorption peak intensity relative to C-CeO₂/ZCS and ZCS, manifesting its robust oxygen-adsorption affinity [53]. The result further confirms that J-CeO₂/ZCS contains additional oxygen-adsorption sites, which can be ascribed to the Janus interfaces with abundant vacancies. This interface offers active sites for O₂ adsorption and activation, which accelerates the

oxygen reduction steps.

To evaluate the influence of CeO₂ on ORR performance, LSV curves and the corresponding electrochemically active surface areas (ECSAs) are determined. The E_{1/2}, E_{onset} and J_L on CeO₂/ZCS increase gradually as the content of CeO₂ increases, however, the excess CeO₂ also lead to a decreased ORR activity (Fig. 4e). Impressively, the kinetic current density (J_k) at 0.9 V follows the order of J-CeO₂/ZCS (1.77 mA cm⁻²) > 0.1CeO₂/ZCS (1.28 mA cm⁻²) > 0.3CeO₂/ZCS (0.41 mA cm⁻²) > ZCS (0.32 mA cm⁻²) (Fig. 4f). ECSAs were measured by CV tests (Fig. S13a-b and Fig. S14) in the non-Faraday reaction region, and the double-layer capacitances (C_{dl}) were linearly fitted [54]. In general, bimetallic sulfide with rich redox couples could effectively activate the oxygen molecules, thereby improving the intrinsic activity for ORR. The ZCS derived from CoZn-BTC_U shows a higher C_{dl} than that derived from CoZn-BTC (Fig. S13c), indicating that the loose and porous structure can expose more electroactive sites. As shown in Fig. 4g, C_{dl} value of the J-CeO₂/ZCS catalyst (prepared with 0.2 mmol Ce(NO₃)₃·6 H₂O) is calculated to be 33 mF cm⁻², much higher than contrast catalysts, indicating the introduced CeO₂ significantly increases the catalytic active sites [55]. The proper CeO₂, possessing good redox reactivity and abundant oxygen vacancy, effectively regulate the structure and electronic energy state of composite catalyst, thus the ORR activity can be greatly enhanced [56]. The durability was evaluated by chronoamperometry in O₂-saturated 0.1 M KOH at 1600 rpm. J-CeO₂/ZCS

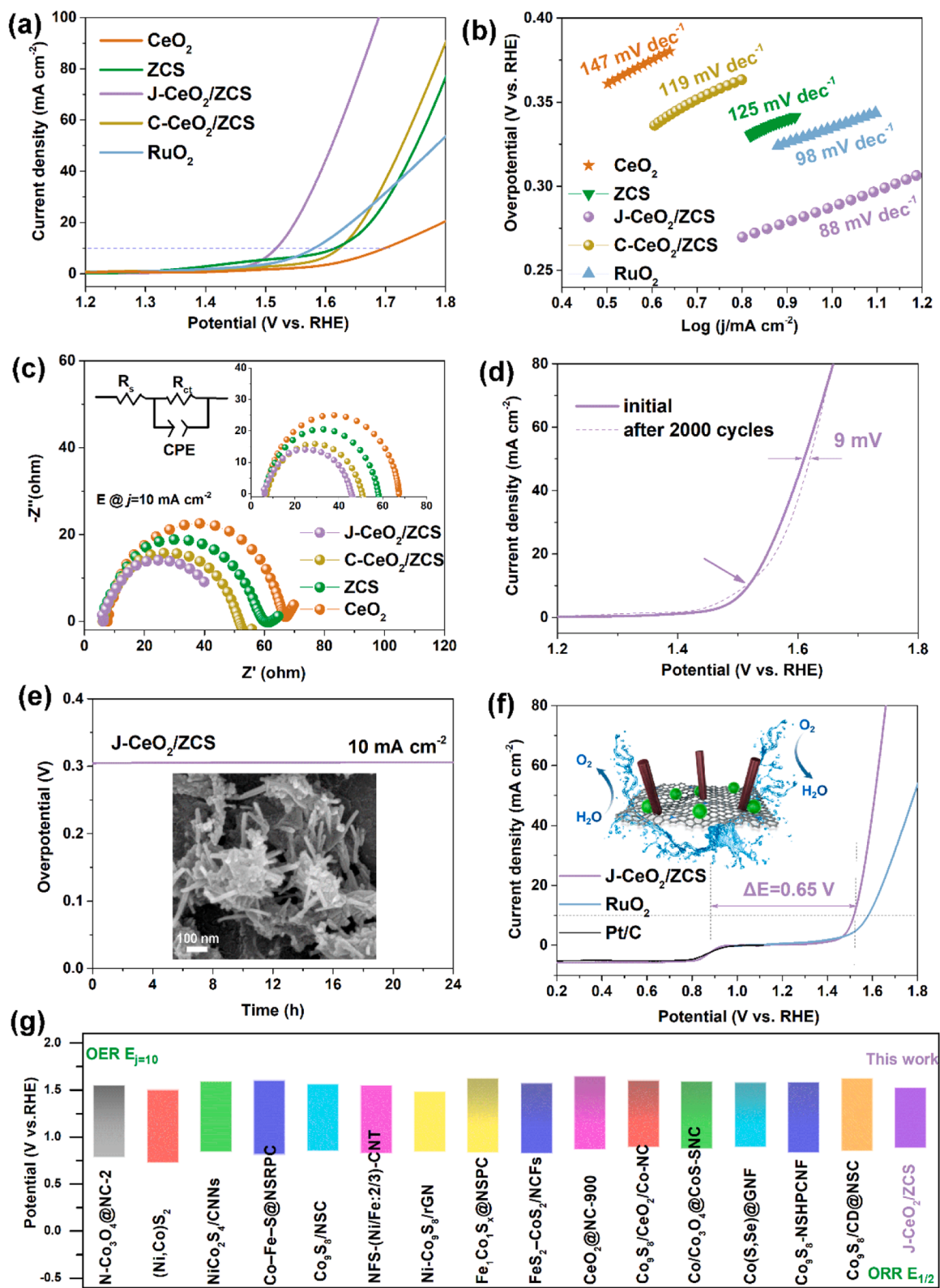


Fig. 5. (a) OER LSV curves of as-prepared catalysts and RuO₂ in 1 M KOH solution, 10 mV s⁻¹, 1600 rpm. (b) the corresponding Tafel plots. (c) EIS spectra of catalysts recorded at the potentials of $J = 10 \text{ mA cm}^{-2}$. (d) LSV curves of initial J-CeO₂/ZCS and tested after 2000 CV cycles. (e) Chronopotentiometry measurement of the J-CeO₂/ZCS at 10 mA cm⁻². The inset is SEM image of J-CeO₂/ZCS after the stability test. (f) ORR and OER bifunctional LSV curves of J-CeO₂/ZCS and Pt/C+RuO₂. (g) Comparison of the bifunctional activity of J-CeO₂/ZCS and some representative electrocatalysts recently reported.

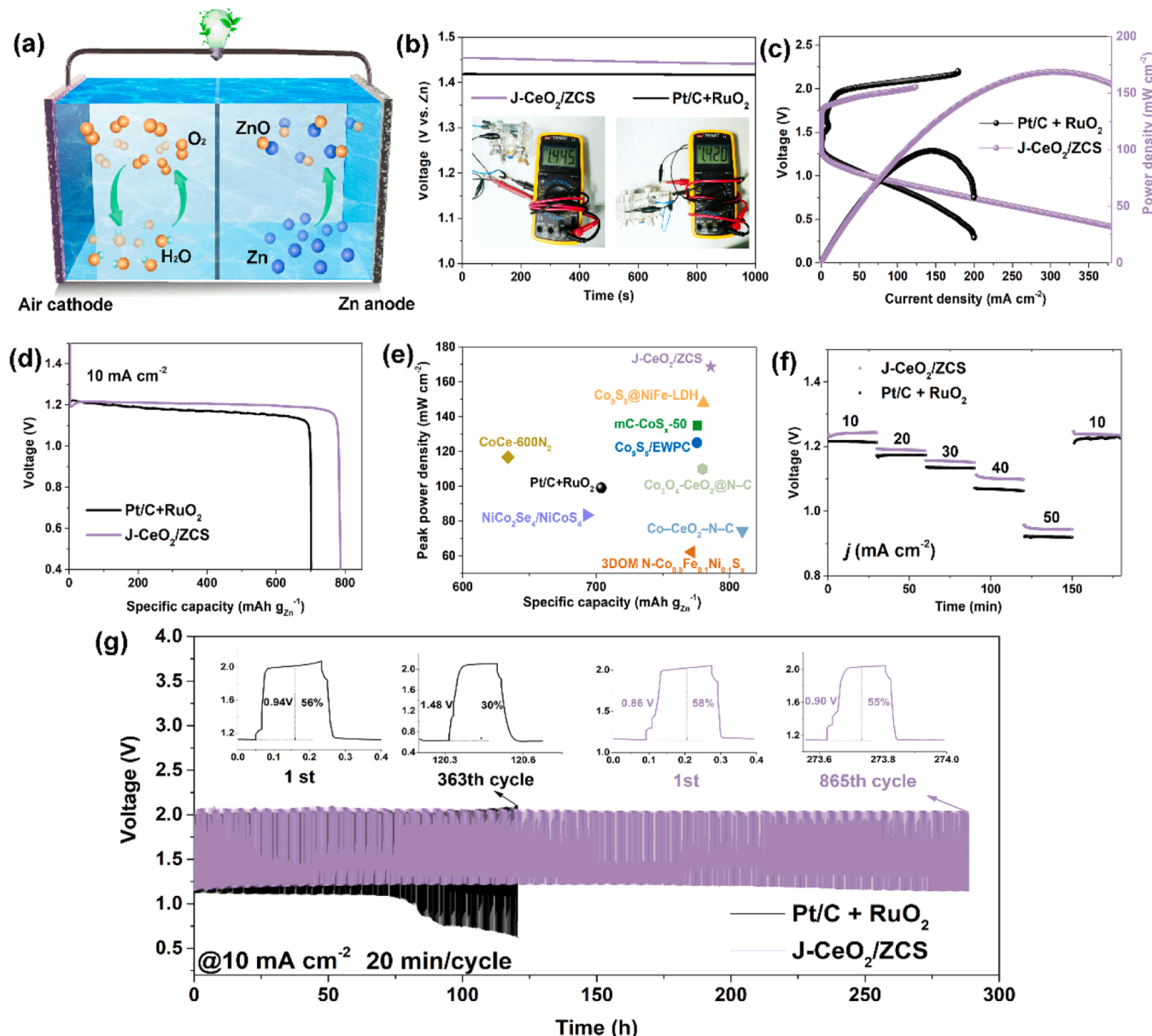


Fig. 6. (a) Schematic configuration of a liquid ZAB. (b) Open circuit voltage curves of ZABs by applying J-CeO₂/ZCS and Pt/C+RuO₂ as air cathode (Inset is the corresponding multimeter screen). (c) Charge/discharge polarization and corresponding power density curves. (d) Discharge curves at a constant current density of 10 mA cm⁻² of ZABs employing J-CeO₂/ZCS and Pt/C+RuO₂ as air cathodes. (e) Comparison of the specific capacity and peak power density of J-CeO₂/ZCS and previously reported TMS- and CeO₂-based catalysts employed for ZABs. (f) Discharge curves at different current densities. (g) Galvanostatic discharge-charge cyclability test of ZABs at 10 mA cm⁻².

(retaining ca. 93% after 18000 s) represents much better stability than that of Pt/C (60%) and ZCS (81%), exhibiting great potential for practical application (Fig. 4h). The intertwined CeO₂ nanorods among the porous ZCS may restrain the loss and aggregation of active species, giving rise to remarkable stability of J-CeO₂/ZCS. According to EIS result (Fig. 4i), the charge-transfer resistance (R_{ct}) of J-CeO₂/ZCS is lower in comparison with other samples, revealing the improved intrinsic conductivity induced by interfacial engineering.

Meanwhile, OER performance of J-CeO₂/ZCS was also conducted in O₂-saturated 1 M KOH. The polarization curve of J-CeO₂/ZCS shows a significantly low operating potential (1.52 V) at 10 mA cm⁻², notably lower than that of commercial RuO₂ (1.58 V) and other comparative catalysts (Fig. 5a). The higher OER activity of J-CeO₂/ZCS was attributed to the improved intrinsic catalytic activity induced by the Janus heterointerfaces and abundant vacancies. The interlaced nanostructure

and vacancies can be well maintained after the OER (Fig. S15). J-CeO₂/ZCS also exhibits the relatively smaller Tafel slope (88 mV dec⁻¹) relative to CeO₂ (147 mV dec⁻¹), ZCS (125 mV dec⁻¹), C-CeO₂/ZCS (119 mV dec⁻¹), and RuO₂ (98 mV dec⁻¹), demonstrating its excellent kinetics toward OER (Fig. 5b) [57]. Turnover frequency (TOF) is another crucial parameter for evaluating the catalytic activity. The J-CeO₂/ZCS catalyst possesses the highest TOF value of ~0.175 s⁻¹ at the overpotential of 350 mV, which is significantly higher than that of ZCS (Fig. S16), representing its superior OER activity. LSV curves of hybrids with different CeO₂ contents for OER were shown in Fig. S17a. J-CeO₂/ZCS also exceeds that of the other catalysts, which can be ascribed to the high oxygen storage capacity of CeO₂ in the composite [58]. However, the excessive CeO₂ (0.3CeO₂/ZCS) may bring about dense structure that reduced ECSA and the gas bubble release on the electrode surface, leading to a decreased OER activity. The OER

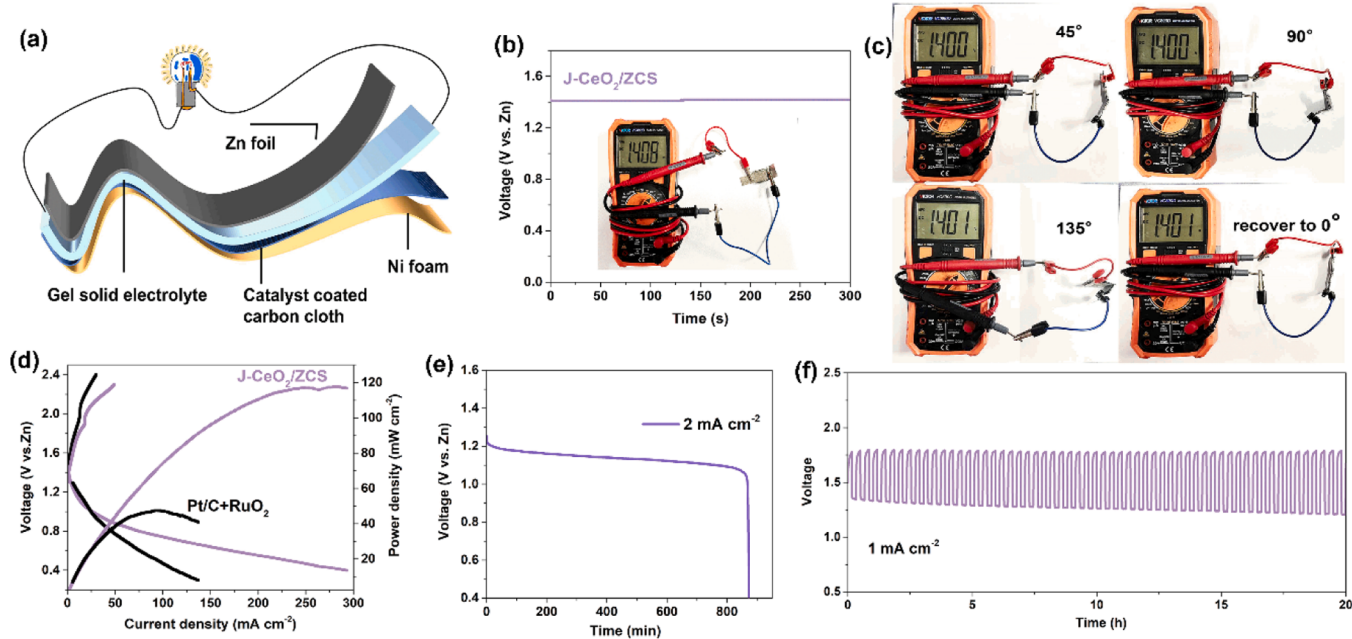


Fig. 7. (a) Schematic illustration of homemade flexible solid-state ZABs. (b) OCV curve of FZAB by applying J-CeO₂/ZCS as the air cathode catalyst. (c) OCV of J-CeO₂/ZCS-based FZABs with different bending angles. (d) Charge/discharge polarization and power density curves of FZABs. (e) Discharge curve of FZAB employing J-CeO₂/ZCS as the air cathode at 2 mA cm⁻². (f) Charge and discharge cycling curve of flexible solid-state Zn-air batteries at 1 mA cm⁻².

polarization curves normalized by the ECSA also confirmed the highest normalized current of J-CeO₂/ZCS, indicating its superior intrinsic activity (Fig. S17b) [59]. Based on the above results, the appropriate content of CeO₂ endows the catalyst with excellent ORR/OER catalytic activity and reaction kinetics. EIS spectra (Fig. 5c) recorded at $E_{j=10}$ indicate the J-CeO₂/ZCS shows a smallest R_{ct} value (Table S3), implying the accelerated electron transfer and electrode/electrolyte charge-transfer during OER [48,60].

OER durability of J-CeO₂/ZCS was evaluated by cycling the potential between 1.4 and 1.6 V for 2000 cycles. Compared with initial LSV curve, J-CeO₂/ZCS obtained after cycling shows the ignorable change, validating its high durability (Fig. 5d). The good durability is further evaluated by chronoamperometry conducted at 10 mA cm⁻² for 24 h. The J-CeO₂/ZCS maintains outstanding stability with negligible potential degradation and shows almost no morphology change after test (Fig. 5e). Furthermore, the potential gap between OER and ORR ($\Delta E = E_{j=10} - E_{1/2}$) can be utilized to evaluate the bifunctional electrocatalytic activity of catalysts. The smaller ΔE value of J-CeO₂/ZCS (0.65 V, as shown in Fig. 5f) was obviously smaller than that of benchmark Pt/C+RuO₂, demonstrating its better bifunctional activity for ORR and OER. Additionally, the ΔE value of J-CeO₂/ZCS is also much smaller than most of the reported same types of bifunctional electrocatalysts (Fig. 5g and Table S2). The considerable ORR and OER performance of the J-CeO₂/ZCS heterostructure should be ascribed to the well-coupled interfaces and the interface induced synergistic effect.

3.3. Liquid zinc-air battery performance

Moreover, J-CeO₂/ZCS is further utilized as air cathode catalyst of home-made ZABs with 6 M KOH containing 0.2 M Zn(Ac)₂ to evaluate its potential under practical application (Fig. 6a). J-CeO₂/ZCS-based ZAB shows a stable open circuit voltage (OCV) of 1.44 V, which is higher than that of Pt/C+RuO₂ (1.42 V) (Fig. 6b). Its peak power density (Fig. 6c) can reach 168.7 mW cm⁻² at 306 mA cm⁻², which is better than that of Pt/C+RuO₂-based ZAB (99.2 mW cm⁻² and 143 mA cm⁻², respectively). In terms of the charge/discharge polarization curves, the J-CeO₂/ZCS-based ZAB shows a narrow charge/discharge voltage gap when compared with that of Pt/C+RuO₂, implying its better

reversibility. Besides, J-CeO₂/ZCS-based ZAB exhibits the specific discharge capacity of 785.9 mAh g_{Zn}⁻¹ at the current density of 10 mA cm⁻², which is superior than the ZAB equipped with Pt/C+RuO₂ (703.9 mAh g_{Zn}⁻¹) (Fig. 6d). Furthermore, it also shows no significant voltage change even applied with relatively higher current density of 20 mA cm⁻² (Fig. S18), indicating its great potential in a stable practical application. Especially, the peak power density and specific capacity of J-CeO₂/ZCS-based ZAB were better than those of the recently reported bifunctional oxygen electrocatalysts (Fig. 6e and Table S4). The stable discharge voltage plots further confirm the superior rate performance of J-CeO₂/ZCS-based ZAB at various current densities, manifesting its rechargeability (Fig. 6f) [61].

The cycle stability of J-CeO₂/ZCS in ZAB was verified by galvanostatic charging-discharging at constant current density of 10 mA cm⁻² (Fig. 6g). The J-CeO₂/ZCS cathode shows a lower initial charge/discharge voltage gap of 0.86 V and the energy efficiency of 58%, exceeding the ZAB equipped with Pt/C+RuO₂ (0.94 V and 56%). Notably, J-CeO₂/ZCS-based ZAB maintains the relatively stable over 865 cycles for ~288 h with negligible change on round-trip efficiency, verifying its robust cycle reversibility. By contrast, Pt/C+RuO₂ cathode dramatically declined after 363 cycles for ~121 h. The outstanding cycling stability mainly originates from the porous structure with intertwined nanorods, which facilitates O₂ diffusion and mass transport. Moreover, synergistic effects between the ZCS/CeO₂ heterostructure and S doping in N-rich carbon with abundant vacancies also improve the oxygen electrocatalytic activities. However, after long-term cycling, the inevitable decay of J-CeO₂/ZCS-based ZAB was caused by the degradation of zinc anode and catalysts oxidation, which induced the loss of active sites and inactivation. In comparison, the Pt/C+RuO₂-based ZAB suffered the detachment of Pt from carbon support and carbon corrosion. To demonstrate the superiority of J-CeO₂/ZCS application, the cycling performance of more reported liquid ZABs based on bifunctional catalysts was also summarized in Table S4.

3.4. All solid-state zinc-air battery performance

As an ideal power sources for portable and wearable electronic equipment, the flexible solid-state ZAB (FZAB) was assembled and

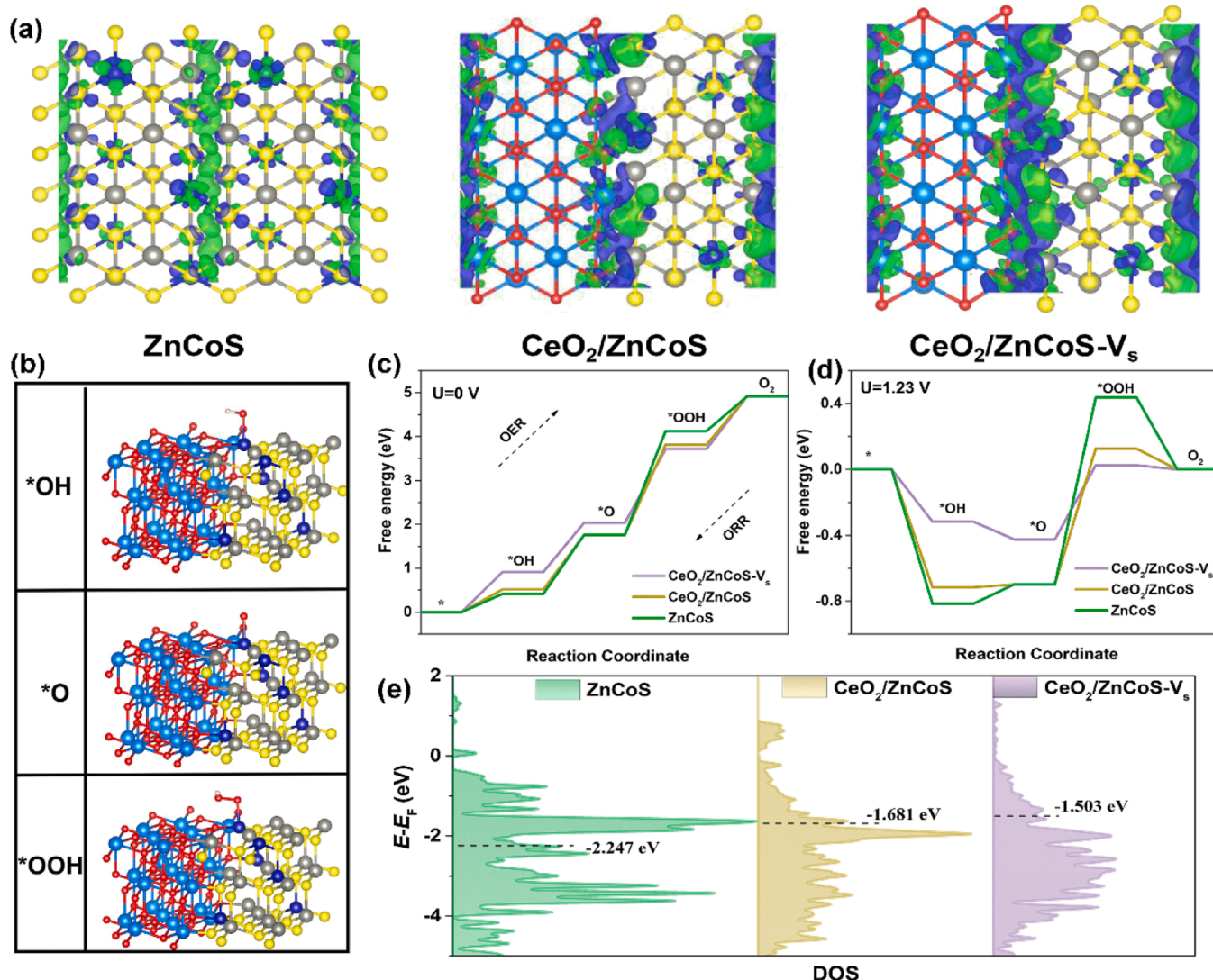


Fig. 8. (a) The electron density difference of ZnCoS, CeO₂/ZnCoS, and CeO₂/ZnCoS-V_s. Green and blue isosurfaces represent the electron accumulation and depletion, respectively. (b) Atomic configurations of *OH, *O, and *OOH adsorbed on CeO₂/ZnCoS-V_s model. Free energy diagrams for OER and ORR on the catalyst models: (c) U = 0 V and (d) U = 1.23 V. (e) PDOS for d orbital of ZnCoS, CeO₂/ZnCoS, and CeO₂/ZnCoS-V_s. The d-band centers of Co atoms are set as dash lines.

evaluated to further extend the practical application of J-CeO₂/ZCS (Fig. 7a). The FZAB equipped with J-CeO₂/ZCS as air electrode shows a stable OCV of ~ 1.40 V (Fig. 7b). Notably, the J-CeO₂/ZCS-based FZAB exhibits negligible changes on OCV when bended from 0° to 135° (Fig. 7c). The J-CeO₂/ZCS-based FZAB also demonstrates a peak power density of 117.6 mW cm⁻², which is much better than that of Pt/C+RuO₂ (47.5 mW cm⁻²) (Fig. 7d). The discharge performance was performed at 2 mA cm⁻² and the J-CeO₂/ZCS-based FZAB could continuously discharge over 880 min with the stable voltage plateau (Fig. 7e). The considerable discharge time and stable voltage can be maintained even conducted at 10 mA cm⁻² (Fig. S19). Simultaneously, J-CeO₂/ZCS electrode also delivers stable voltage plateaus with the gradually increased current densities (Fig. S20). When the current density decreased to 0.2 mA cm⁻², the voltage of FZAB can be recovered to its initial state, indicating its high-rate performance. As shown in Fig. 7f, the rechargeability of FZAB was evaluated at 1 mA cm⁻² with 20 min of galvanostatic charging/discharging for each cycle, confirming its application prospect for future flexible electronic equipment.

3.5. DFT calculation analysis

Density functional theory (DFT) calculations are conducted to

expound the reason for enhanced OER and ORR performance on the CeO₂/ZnCoS interface. In XRD pattern of J-CeO₂/ZCS, the diffraction peaks of CeO₂ (111) plane and Zn_{0.76}Co_{0.24}S (111) plane show the highest intensity that are in accord with the observation in HRTEM, providing reference to the combination of planes. Therefore, the theoretical models of ZnCoS, CeO₂/ZnCoS, and CeO₂/ZnCoS-V_s (V_s represents sulfur vacancy) are displayed in Fig. S21. The charge density difference of three models exhibit that the strong charge redistribution occurs at the CeO₂/ZnCoS-V_s heterointerface (Fig. 8a), which regulates the interfacial electronic structure and optimizes the absorption/desorption of oxygen intermediates [62].

ORR mechanism is generally described as a 4-electron transfer pathway and involves the adsorption O₂ to *OOH followed by further reduction to *O and *OH [21]. OER is considered as the corresponding reverse process. To verify the synergistic effect of the heterostructures for optimizing the ORR pathway, Co site was chosen as the adsorption and desorption of oxygen intermediates (HOO*, O*, and HO*) and Gibbs free energy for each step was calculated. The interaction of three catalytic models with oxygen intermediates are shown in Fig. S22 and Fig. 8b. At zero potential (U = 0 V), the downhill Gibbs free energy decreases as the oxidation state of oxygen decreases, revealing that the electron transfer steps on all the models are exothermic that means

spontaneous process [63]. Moreover, the ΔG of $^{*}\text{OOH}$ and $^{*}\text{OH}$ is emerged as a critical descriptor of OER activity with an optimum value of 2.46 eV [64]. DFT results show that the ΔG ($^{*}\text{OOH}$ – $^{*}\text{OH}$) of $\text{CeO}_2/\text{ZnCoS-V}_s$ is 2.79 eV while those for ZnCoS and $\text{CeO}_2/\text{ZnCoS}$ are 3.74 and 3.29 eV, respectively, indicating $\text{CeO}_2/\text{ZnCoS-V}_s$ shows ideal OER kinetics because it is closer to 2.46 eV (Fig. 8c). For another, $\text{CeO}_2/\text{ZnCoS-V}_s$ possesses more considerable exothermic proton–electron transfer steps, indicating an enhanced ORR activity due to the low overpotential (0.32 V) for the rate-determining step (RDS) of $^{*}\text{OH} \rightarrow \text{OH}^-$. In contrast, both ZnCoS and $\text{CeO}_2/\text{ZnCoS}$ show the much higher overpotential of 0.82 V and 0.72 V for RDS, respectively. Besides, at the equilibrium potential of 1.23 V (Fig. 8d), the lower limiting barrier can be achieved on $\text{CeO}_2/\text{ZnCoS-V}_s$ for the RDS. The above results verify the $\text{CeO}_2/\text{ZnCoS-V}_s$ heterostructure is beneficial to improve the OER/ORR activity.

Density of states (DOS) in Fig. S23 show various orbital hybridization in three catalytic models, further revealing the strong electronic interaction between CeO_2 and ZnCoS . The calculated partial density of state (PDOS) (Fig. 8e) reveal the up-shifted d band center of Co in the $\text{CeO}_2/\text{ZnCoS-V}_s$ with a decreased intensity, which result in a weaker binding capability to reactant O_2 and better electron transferring [65]. It also suggests the electrical and chemical modulation in the $\text{CeO}_2/\text{ZnCoS-V}_s$ heterointerface, which exerts positive influence on oxygen electrocatalysis. Theoretical calculation result not only confirms that the electronic structure of active site was effectively regulated by interfacial engineering, but also gives the strong evidence for the bifunctional properties of J- CeO_2/ZCS catalyst.

4. Conclusions

In conclusion, interfacial engineering strategy was applied to develop Janus heterostructure of CeO_2/ZCS embedded in N-doped carbon. The CeO_2/ZCS heterointerface induces the electronic redistribution of active site and generates more active sites, which significantly contribute to improving the intrinsic activity. Accordingly, the optimal J- CeO_2/ZCS exerts the strong interfacial effect of CeO_2 and ZCS, leading to superior electrocatalytic activity for ORR and OER as well as robust stability. More impressively, when assembled in rechargeable aqueous ZABs, the J- CeO_2/ZCS -based ZABs exhibit considerable power density, specific capacity and excellent cycling stability, surpassing the noble-metal counterparts and state-of-the-art catalysts previously reported. It also holds great potential in rechargeable and flexible ZAB devices. This work affords idea for the interfacial construction and nanostructure engineering on efficient electrocatalysts in energy systems.

CRediT authorship contribution statement

Jie Zhang: Conceptualization, Data curation, Methodology, Writing-original draft. **Xinran Dong:** Data curation, Methodology. **Gang Wang:** Writing-review & editing. **Jinwei Chen:** Data curation, Investigation. **Ruilin Wang:** Project administration, Funding acquisition.

Declaration of Competing Interest

The authors declare that they have no known competing financial interests or personal relationships that could have appeared to influence the work reported in this paper.

Data Availability

Data will be made available on request.

Acknowledgements

This study was supported by Natural Science Foundation of Sichuan Province (2022NSFSC1192), Fundamental Research Funds for Central

Universities (20826041E4280) and Creative Project of Engineering Research Center of Alternative Energy Materials & Devices in Sichuan University (AEMD-C202203). The authors would like to thank Dr. Wenwu Wang from Central Lab of College of Materials Science and Engineering for the BET measurement. We also thank Dr. Xiaoshan Zhang for the TGA measurement.

Appendix A. Supporting information

Supplementary data associated with this article can be found in the online version at doi:10.1016/j.apcatb.2023.123459.

References

- [1] F. Jaouen, E. Proietti, M. Lefèvre, R. Chenitz, J.-P. Dodelet, G. Wu, H.T. Chung, C. M. Johnston, P. Zelenay, Recent advances in non-precious metal catalysis for oxygen-reduction reaction in polymer electrolyte fuelcells, *Energy Environ. Sci.* 4 (2011) 114–130.
- [2] X. Wen, Q. Zhang, J. Guan, Applications of metal–organic framework-derived materials in fuel cells and metal-air batteries, *Coord. Chem. Rev.* 409 (2020), 213214.
- [3] T. Zhou, N. Zhang, C. Wu, Y. Xie, Surface/interface nanoengineering for rechargeable Zn-air batteries, *Energy Environ. Sci.* 13 (2020) 1132–1153.
- [4] Y. Ren, P. Ye, J. Chen, H. Wang, J. Ning, J. Shen, Y. Zhong, Y. Hu, Fabrication of copper–cobalt heterostructures confined inside N-doped carbon nanocages for long-lasting Zn-air batteries, *J. Power Sources* 545 (2022), 231908.
- [5] S. Li, D. Liu, G. Wang, P. Ma, X. Wang, J. Wang, R. Ma, Vertical 3D nanostructures boost efficient hydrogen production coupled with glycerol oxidation under alkaline conditions, *Nano-Micro Lett.* 15 (2023) 189.
- [6] A. Wang, C. Zhao, M. Yu, W. Wang, Trifunctional Co nanoparticle confined in defect-rich nitrogen-doped graphene for rechargeable Zn-air battery with a long lifetime, *Appl. Catal. B: Environ.* 281 (2021), 119514.
- [7] Z. Lin, Z. Wang, J. Gong, T. Jin, S. Shen, Q. Zhang, J. Wang, W. Zhong, Reversed spillover effect activated by Pt atom dimers boosts alkaline hydrogen evolution reaction, *Adv. Funct. Mater.* (2023) 2307510.
- [8] D.A. Kuznetsov, B. Han, Y. Yu, R.R. Rao, J. Hwang, Y. Román-Leshkov, Y. Shao-Horn, Tuning redox transitions via inductive effect in metal oxides and complexes, and implications in oxygen electrocatalysis, *Joule* 2 (2018) 225–244.
- [9] H. Wang, J. Li, K. Li, Y. Lin, J. Chen, L. Gao, V. Nicolosi, X. Xiao, J.M. Lee, Transition metal nitrides for electrochemical energy applications, *Chem. Soc. Rev.* 50 (2021) 1354–1390.
- [10] W. Peng, Y. Wang, X. Yang, L. Mao, J. Jin, S. Yang, K. Fu, G. Li, Co_3S_8 nanoparticles embedded in multiple doped and electrospun hollow carbon nanofibers as bifunctional oxygen electrocatalysts for rechargeable zinc-air battery, *Appl. Catal. B: Environ.* 268 (2020), 118437.
- [11] D.H. Wu, H. Huang, M. Ul Haq, L. Zhang, J.J. Feng, A.J. Wang, Lignin-derived iron carbide/Mn, N, S-codoped carbon nanotubes as a high-efficiency catalyst for synergistically enhanced oxygen reduction reaction and rechargeable zinc-air battery, *J. Colloid Interface Sci.* 647 (2023) 1–11.
- [12] Z. Han, J.J. Feng, Y.Q. Yao, Z.G. Wang, L. Zhang, A.J. Wang, Mn, N, P-tridoped bamboo-like carbon nanotubes decorated with ultrafine $\text{Co}_2\text{P}/\text{FeCo}$ nanoparticles as bifunctional oxygen electrocatalyst for long-term rechargeable Zn-air battery, *J. Colloid Interface Sci.* 590 (2021) 330–340.
- [13] W. Zhang, Y.P. Chen, L. Zhang, J.J. Feng, X.S. Li, A.J. Wang, Theophylline-regulated pyrolysis synthesis of nitrogen-doped carbon nanotubes with iron-cobalt nanoparticles for greatly boosting oxygen reduction reaction, *J. Colloid Interface Sci.* 626 (2022) 653–661.
- [14] A.P. Tiwari, D. Kim, Y. Kim, H. Lee, Bifunctional oxygen electrocatalysis through chemical bonding of transition metal chalcogenides on conductive carbons, *Adv. Energy Mater.* 7 (2017) 1602217.
- [15] J.-H. Jang, M. Lee, S. Park, J.-M. Oh, J.K. Park, S.-M. Paek, Long-term cycling stability of a SnS_2 -based covalent organic nanosheet anode for lithium-ion batteries, *J. Mater. Chem. A* 11 (2023) 13320–13330.
- [16] Y.P. Zhu, C. Guo, Y. Zheng, S.-Z. Qiao, Surface and interface engineering of noble-metal-free electrocatalysts for efficient energy conversion processes, *Acc. Chem. Res.* 50 (2017) 915–923.
- [17] X. Yuan, J. Yin, Z. Liu, X. Wang, C. Dong, W. Dong, M.S. Riaz, Z. Zhang, M.-Y. Chen, F. Huang, Charge-transfer-promoted high oxygen evolution activity of $\text{Co}@\text{Co}_3\text{S}_8$ core–shell nanochains, *ACS Appl. Mater. Inter.* 10 (2018) 11565–11571.
- [18] W. Shang, W. Yu, X. Xiao, Y. Ma, Y. He, P. Tan, Free-standing electrode of core–shell-structured $\text{NiO}@\text{Co}_3\text{S}_4$ for high-performance hybrid Zn–Co/air batteries, *Energy Fuels* 36 (2022) 1121–1128.
- [19] L. Bo, W. Shi, F. Nian, Y. Hu, L. Pu, P. Li, Z. Zhang, J. Tong, Interface engineering of $\text{Co}_3\text{S}_4@\text{Co}_3\text{O}_4/\text{N}$, S-doped carbon core@shell nanostructures serve as an excellent bifunctional ORR/OER electrocatalyst for rechargeable Zn-air battery, *Sep. Purif. Technol.* 307 (2023), 122536.
- [20] P. Kulkarni, S.K. Nataraj, R.G. Balakrishna, D.H. Nagaraju, M.V. Reddy, Nanostructured binary and ternary metal sulfides: synthesis methods and their application in energy conversion and storage devices, *J. Mater. Chem. A* 5 (2017) 22040–22094.

[21] J. Cai, H. Liu, Y. Luo, Y. Xiong, L. Zhang, S. Wang, K. Xiao, Z.-Q. Liu, Single-phase bimetal sulfide or metal sulfide heterojunction: Which one is better for reversible oxygen electrocatalyst? *J. Energy Chem.* 74 (2022) 420–428.

[22] N.L.D. Sui, J.-M. Lee, Versatile Janus architecture for electrocatalytic applications, *Small* 19 (2023) 2205940.

[23] F. Ma, S. Wang, X. Gong, X. Liu, Z. Wang, P. Wang, Y. Liu, H. Cheng, Y. Dai, Z. Zheng, B. Huang, Highly efficient electrocatalytic hydrogen evolution coupled with upcycling of microplastics in seawater enabled via $\text{Ni}_3\text{N}/\text{W}_5\text{N}_4$ janus nanostructures, *Appl. Catal. B: Environ.* 307 (2022), 121198.

[24] X. Li, H. Zhang, X. Li, Q. Hu, C. Deng, X. Jiang, H. Yang, C. He, Janus heterostructure of cobalt and iron oxide as dual-functional electrocatalysts for overall water splitting, *Nano Res* 16 (2022) 2245–2251.

[25] H. Liu, J. Cheng, W. He, Y. Li, J. Mao, X. Zheng, C. Chen, C. Cui, Q. Hao, Interfacial electronic modulation of Ni_3S_2 nanosheet arrays decorated with Au nanoparticles boosts overall water splitting, *Appl. Catal. B: Environ.* 304 (2022), 120935.

[26] Q. Lu, H. Wu, X. Zheng, Y. Cao, J. Li, Y. Wang, H. Wang, C. Zhi, Y. Deng, X. Han, W. Hu, Controllable constructing Janus homologous heterostructures of transition metal alloys/sulfides for efficient oxygen electrocatalysis, *Adv. Energy Mater.* 12 (2022) 2202215.

[27] Y. Feng, N. Ran, X. Wang, Q. Liu, J. Wang, L. Liu, K. Suenaga, W. Zhong, R. Ma, J. Liu, Nanoparticulate $\text{WN}/\text{Ni}_3\text{C}$ coupling in ceramic coatings for boosted urea electro-oxidation, *Adv. Energy Mater.* (2023) 2302452.

[28] Y. Du, D. Liu, T. Li, Y. Yan, Y. Liang, S. Yan, Z. Zou, A phase transformation-free redox couple mediated electrocatalytic oxygen evolution reaction, *Appl. Catal. B: Environ.* 306 (2022), 121146.

[29] P. Zhou, G. Hai, G. Zhao, R. Li, X. Huang, Y. Lu, G. Wang, CeO_2 as an “electron pump” to boost the performance of Co_4N in electrocatalytic hydrogen evolution, oxygen evolution and biomass oxidation valorization, *Appl. Catal. B: Environ.* 325 (2023), 122364.

[30] M. Zhang, D. Hu, Z. Xu, B. Liu, M. Boubeche, Z. Chen, Y. Wang, H. Luo, K. Yan, Facile synthesis of Ni-, Co-, Cu-metal organic frameworks electrocatalyst boosting for hydrogen evolution reaction, *J. Mater. Sci. Technol.* 72 (2021) 172–179.

[31] H. Wang, X. Zhang, F. Yin, W. Chu, B. Chen, Coordinately unsaturated metal-organic framework as an unpyrolyzed bifunctional electrocatalyst for oxygen reduction and evolution reactions, *J. Mater. Chem. A* 8 (2020) 22111–22123.

[32] T. Li, T. Lu, Y. Li, J. Yin, Y. Tang, M. Zhang, H. Pang, L. Xu, J. Yang, Y. Zhang, Interfacial engineering-induced electronic regulation drastically enhances the electrocatalytic oxygen evolution: Immobilization of Janus-structured NiS/NiO nanoparticles onto carbon nanotubes/nanofiber-integrated superstructures, *Chem. Eng. J.* 428 (2022), 131094.

[33] A. Zehtab Yazdi, K. Chizari, A.S. Jalilov, J. Tour, U. Sundararaj, Helical and Dendritic unzipping of carbon nanotubes: A route to nitrogen-doped graphene nanoribbons, *ACS Nano* 9 (2015) 5833–5845.

[34] Y. Liao, R. He, W. Pan, Y. Li, Y. Wang, J. Li, Y. Li, Lattice distortion induced Ce-doped NiFe-LDH for efficient oxygen evolution, *Chem. Eng. J.* 464 (2023), 142669.

[35] X. Feng, Q. Jiao, Q. Li, Q. Shi, Z. Dai, Y. Zhao, H. Li, C. Feng, W. Zhou, T. Feng, NiCo_2S_4 spheres grown on N,S co-doped rGO with high sulfur vacancies as superior oxygen bifunctional electrocatalysts, *Electrochim. Acta* 331 (2020), 135356.

[36] X. Zheng, Y. Cao, X. Zheng, M. Cai, J. Zhang, J. Wang, W. Hu, Engineering interface and oxygen vacancies of $\text{Ni}_x\text{Co}_{1-x}\text{Se}_2$ to boost oxygen catalysis for flexible Zn-air batteries, *ACS Appl. Mater. Inter.* 11 (2019) 27964–27972.

[37] H. Wang, X. Bo, Y. Zhang, L. Guo, Sulfur-doped ordered mesoporous carbon with high electrocatalytic activity for oxygen reduction, *Electrochim. Acta* 108 (2013) 404–411.

[38] D. Wang, Y.-P. Deng, Y. Zhang, Y. Zhao, G. Zhou, L. Shui, Y. Hu, M. Shakouri, X. Wang, Z. Chen, Defect engineering on three-dimensionally ordered macroporous phosphorus doped $\text{Co}_3\text{O}_{4-\delta}$ microspheres as an efficient bifunctional electrocatalyst for Zn-air batteries, *Energy Storage Mater.* 41 (2021) 427–435.

[39] W. Lu, M. Yuan, J. Chen, J. Zhang, L. Kong, Z. Feng, X. Ma, J. Su, J. Zhan, Synergistic Lewis acid-base sites of ultrathin porous Co_3O_4 nanosheets with enhanced peroxidase-like activity, *Nano Res* 14 (2021) 3514–3522.

[40] J. Zhang, C. Yu, J. Lang, Y. Zhou, B. Zhou, Y.H. Hu, M. Long, Modulation of Lewis acidic-basic sites for efficient photocatalytic H_2O_2 production over potassium intercalated tri-s-triazine materials, *Appl. Catal. B: Environ.* 277 (2020), 119225.

[41] Y. Hu, Z. Li, Z. Wang, X. Wang, W. Chen, J. Wang, W. Zhong, R. Ma, Suppressing local dendrite hotspots via current density redistribution using a superlithiophilic membrane for stable lithium metal anode, *Adv. Sci.* 10 (2023) 2206995.

[42] W. Zheng, J. Lv, H. Zhang, H.-X. Zhang, J. Zhang, Co_9S_8 integrated into nitrogen/sulfur dual-doped carbon nanofibers as an efficient oxygen bifunctional electrocatalyst for Zn-air batteries, *Sustain. Energ. Fuels* 4 (2020) 1093–1098.

[43] X. He, X. Yi, F. Yin, B. Chen, G. Li, H. Yin, Less active CeO_2 regulating bifunctional oxygen electrocatalytic activity of $\text{Co}_3\text{O}_4@\text{N}$ -doped carbon for Zn-air batteries, *J. Mater. Chem. A* 7 (2019) 6753–6765.

[44] K.R. Yoon, J.M. Kim, K.A. Lee, C.-K. Hwang, S.G. Akpe, Y.J. Lee, J.P. Singh, K. H. Chae, S.S. Jang, H.C. Ham, J.Y. Kim, Activity-stability benefits of Pt/C fuel cell electrocatalysts prepared via remote CeO_2 interfacial doping, *J. Power Sources* 496 (2021), 229798.

[45] S. Ramakrishnan, M. Karuppannan, M. Vinothkannan, K. Ramachandran, O. J. Kwon, D.J. Yoo, Interfaces, Ultrafine Pt nanoparticles stabilized by MoS_2/N -Doped reduced graphene oxide as a durable electrocatalyst for alcohol oxidation and oxygen reduction reactions, *ACS Appl. Mater. Interfaces* 13 (2019) 12504–12515.

[46] P. Yang, F. Kong, X. Sui, L. Zhao, Y. Qiu, H. Zhang, Z. Wang, Hollow structured $\text{Zn}_0.76\text{Co}_{0.24}\text{S}-\text{Co}_9\text{S}_8$ composite with two-phase synergistic effect as bifunctional catalysts, *Int. J. Hydrog. Energ.* 47 (2022) 8811–8819.

[47] Y. Yang, Y.X. Yin, S. Xin, Y.G. Guo, L.J. Wan, Ionothermal synthesis of sulfur-doped porous carbons hybridized with graphene as superior anode materials for lithium-ion batteries, *Chem. Commun.* 48 (2012) 10663–10665.

[48] Y. Niu, X. Teng, S. Gong, X. Liu, M. Xu, Z. Chen, Boosting oxygen electrocatalysis for flexible zinc-air batteries by interfacing iron group metals and manganese oxide in porous carbon nanowires, *Energy Storage Mater.* 43 (2021) 42–52.

[49] Y. Luo, Y. Chen, Y. Xue, J. Chen, G. Wang, R. Wang, M. Yu, J. Zhang, Electron. Struct. Regul. iron phthalocyanine Induc. Anchor Heteroat. -doping Carbon Sphere Effic. Oxyg. Reduct. React. Al-air Battery 18 (2022) 2105594.

[50] S. Ramakrishnan, J. Balamurugan, M. Vinothkannan, A.R. Kim, S. Sengodan, D. J. Yoo, Nitrogen-doped graphene encapsulated FeCoMoS nanoparticles as advanced trifunctional catalyst for water splitting devices and zinc-air batteries, *Appl. Catal. B: Environ.* 279 (2020), 119381.

[51] L. Li, B. Gao, S. Xu, Q. Xu, Strong ferromagnetic manipulation of SrTiO_3 from CO_2 -straining effect on electronic structure modulation, *Small* 19 (2023) 2300765.

[52] H. Pan, X. Huang, Z. Lu, Z. Zhang, B. An, D. Wu, T. Wang, X. Chen, F. Cheng, Dual oxidation and sulfurization enabling hybrid $\text{Co}/\text{Co}_3\text{O}_4@\text{CoS}$ in S/N-doped carbon matrix for bifunctional oxygen electrocatalysis and rechargeable Zn-air batteries, *Chem. Eng. J.* 419 (2021), 129619.

[53] J. Wang, A. Yoshida, P. Wang, T. Yu, Z. Wang, X. Hao, A. Abudula, G. Guan, Catalytic oxidation of volatile organic compound over cerium modified cobalt-based mixed oxide catalysts synthesized by electrodeposition method, *Appl. Catal. B: Environ.* 271 (2020), 118941.

[54] R. Ma, G. Lin, Q. Ju, W. Tang, G. Chen, Z. Chen, Q. Liu, M. Yang, Y. Lu, J. Wang, Edge-sited Fe-N₄ atomic species improve oxygen reduction activity via boosting O_2 dissociation, *Appl. Catal. B: Environ.* 265 (2020), 118593.

[55] L. Yan, Z. Xu, X. Liu, S. Mahmood, J. Shen, J. Ning, S. Li, Y. Zhong, Y. Hu, Integrating trifunctional Co@NC-CNTs@NiFe-LDH electrocatalysts with arrays of porous triangle carbon plates for high-power-density rechargeable Zn-air batteries and self-powered water splitting, *Chem. Eng. J.* 446 (2022), 137049.

[56] X. Xu, J. Xie, B. Liu, R. Wang, M. Liu, J. Zhang, J. Liu, Z. Cai, J. Zou, PBA-derived FeCo alloy with core-shell structure embedded in 2D N-doped ultrathin carbon sheets as a bifunctional catalyst for rechargeable Zn-air batteries, *Appl. Catal. B: Environ.* 316 (2022), 121687.

[57] S. Wang, H. Wang, C. Huang, P. Ye, X. Luo, J. Ning, Y. Zhong, Y. Hu, Trifunctional electrocatalyst of N-doped graphitic carbon nanosheets encapsulated with CoFe alloy nanocrystals: The key roles of bimetal components and high-content graphitic-N, *Appl. Catal. B: Environ.* 298 (2021), 120512.

[58] J. Xia, H. Zhao, B. Huang, L. Xu, M. Luo, J. Wang, F. Luo, Y. Du, C.H. Yan, Efficient optimization of electron/oxygen pathway by constructing ceria/hydroxide interface for highly active oxygen evolution reaction, *Adv. Funct. Mater.* 30 (2020) 1908367.

[59] L. Yan, B. Xie, C. Yang, Y. Wang, J. Ning, Y. Zhong, Y. Hu, Engineering self-supported hydrophobic-aerophilic air cathode with $\text{CoS}/\text{Fe}_3\text{S}_4$ nanoparticles embedded in S, N co-doped carbon plate arrays for long-life rechargeable Zn-air batteries, *Adv. Energy Mater.* 13 (2023) 2204245.

[60] K. Kim, K. Min, Y. Go, Y. Lee, S.E. Shim, D. Lim, S.-H. Baeck, FeCo alloy nanoparticles embedded in N-doped carbon supported on highly defective ketjenblack as effective bifunctional electrocatalysts for rechargeable Zn-air batteries, *Appl. Catal. B: Environ.* 315 (2022), 121501.

[61] N.K. Wagh, S.S. Shinde, C.H. Lee, J.-Y. Jung, D.-H. Kim, S.-H. Kim, C. Lin, S.U. Lee, J.-H. Lee, Densely colonized isolated Cu-N single sites for efficient bifunctional electrocatalysts and rechargeable advanced Zn-air batteries, *Appl. Catal. B: Environ.* 268 (2020), 118746.

[62] Z. Wang, X. Liao, M. Zhou, F. Huang, K.A. Owusu, J. Li, Z. Lin, Q. Sun, X. Hong, C. Sun, Y.-B. Cheng, Y. Zhao, L. Mai, Interfacial and vacancies engineering of copper nickel sulfide for enhanced oxygen reduction and alcohols oxidation activity, *Energy Environ. Mater.* 6 (2023), e12409.

[63] M. Xie, Y. Zhou, Z. Wang, H. Wang, D. Yan, B. Han, S. Zhang, C. Deng, Heterostructured hollow fibers stitched together from nickel sulfides capped S, N-codoped carbon nanotubes as a trifunctional electrode for flexible hybrid Zn batteries, *Chem. Eng. J.* 431 (2022), 133920.

[64] I.C. Man, H.-Y. Su, F. Calle-Vallejo, H.A. Hansen, J.I. Martínez, N.G. Inoglu, J. Kitchin, T.F. Jaramillo, J.K. Norskov, J. Rossmeisl, Universality in oxygen evolution electrocatalysis on oxide surfaces, *ChemCatChem* 3 (2011) 1159–1165.

[65] Y. Jia, X. Xiong, D. Wang, X. Duan, K. Sun, Y. Li, L. Zheng, W. Lin, M. Dong, G. Zhang, W. Liu, X. Sun, Atomically dispersed Fe-N₄ modified with precisely located S for highly efficient oxygen reduction, *Nano-Micro Lett.* 12 (2020) 116.